Floquet engineering in plasmonic tunnel junctions

Miguel Varea[1†], David Mateos[1,2†] Orazio La Rocca[3,4], Koen Lauwaet[1], Daniel Granados[1], Rodolfo Miranda[1,2], Antonio Isaac Fernández-Domínguez[5,6], Nicola Lo Gullo[3,4], Roberto Otero[1,2,6*], Alberto Martin-Jimenez[1*]*

Supplementary Information

I. Floquet model

Following Refs[1,2] we modeled the vacuum gap between tip and sample as a one-dimensional quantum well, with the tip and the sample treated as two metallic reservoirs with Fermi energies $E_{F,s}$ and $E_{F,t}$ and work functions Φ_s and Φ_t. The external bias voltage is taken to be the difference between the two Fermi energies and is defined by the relation $E_{F,t} = E_{F,s} + eV_{bias}$.

In constant-current STM measurements, the tip position depends on the applied bias. We call z_0 the width of the gap when the tip is set to the base current (smallest cavity). For each value of V_{bias} the tip retracts by a distance $\Delta z(V_{bias})$, effectively increasing the width of the quantum well. The electronic states in the vacuum gap can thus be obtained by solving the time-independent Schrödinger equation:

$$\left[\frac{-\hbar^2}{2m}\frac{d^2}{dz^2} + U(z, V_{bias})\right]\psi(z, V_{bias}) = E_n\psi(z, V_{bias}),$$

where the potential has three contributions $U(z, V_{bias}) = U_{tip} + U_{sample} + U_{tip-sample}$:

The tip image potential:

$$U_{tip} = \frac{-e^2}{16\pi\epsilon_0}\frac{1}{z_0 + \Delta z(V_{bias}) - z}$$

The sample image potential:

$$U_s(z) = \begin{cases} \dfrac{-e^2}{16\pi\varepsilon_0}\dfrac{1}{z - z_{im}} & |z| > z_{im} \\ -U_0 & \end{cases}$$

where z_{im} is the position of the image charge and $U_0 < \Phi_s$.

The tip-sample potential was computed within the sphere–plane approximation using the image charge method. It is influenced by geometrical factors such as the tip radius in spherical approximation, the tip-sample distance, and the position of the image plane z_{im}. A typical potential is plotted in Fig S1a.

To account for the variation in tip-sample distance with bias voltage, we numerically solve the Schrödinger equation using the function $\Delta z(V_{bias})$ obtained from the experimental measurements.

Within this framework, a peak in tunneling spectroscopy occurs when a quantized eigenstate of the well aligns with the tip Fermi level:

$$E_n(V_{bias}) = E_{F,t} = E_{F,s} + eV_{bias}$$

This condition is used to extract the dark states (the field-emission resonances, FERs of the dark cavity).

The effect of an external laser field is introduced through a time-dependent perturbation. Using the minimal substitution, the laser-driven Hamiltonian takes the form:

$$H_{tot} = \frac{(p + eA(t))^2}{2m_e} + U(V_{bias})$$

Where e and m_e are the charge and mass of the electron respectively. In the Coulomb Gauge and using our 1d model (assuming a spatially uniform potential vector along the z direction), the Hamiltonian reads:

$$H_{tot} = H_0 + e\frac{p_z A_z}{m_e} + \frac{e^2 A_z^2}{2m_e}$$

where H_0 is the static Hamiltonian. Projecting it on the unperturbed basis, one finds:

$$H_{tot} = \sum_n \left(E_n + \frac{e^2 A^2(t)}{2m_e}\right)|n\rangle\langle n|, - + e\frac{A(t)}{m_e}\sum_{n,n'}\langle n|p_z|n'\rangle|n\rangle\langle n'|$$

We consider a monochromatic drive: $A(t) = A_0 \sin(\omega_L t)$. The bare coupling strength is given by $g_{n,n'} = eA_0\langle n|p_z|n'\rangle/m_e$ and, for typical experimental parameters, it is of the order of 10^{-5} eV, indicating that the laser field alone is insufficient to significantly modify the tunneling spectrum. However, when the driving frequency is close to resonant modes of the STM junction (e.g., plasmonic or cavity-like excitations), the local field can be strongly enhanced. This effect is captured phenomenologically by introducing an enhancement factor γ, such that $A_{cav} = \gamma A_0$.

In the weak-to-intermediate driving regime considered here, we neglect the diamagnetic term, which induces mainly a rigid energy shift, and retain only the paramagnetic contribution. We checked that this is the case through all our simulations. The effective Hamiltonian reads:

$$H(t) = \sum_n E_n |n\rangle\langle n| + \gamma \sin(\omega_L t)\sum_{n,n'} g_{n,n'}|n\rangle\langle n'|$$

To extract the correct bright resonances, we employ Floquet theory. The solution of the time-dependent Schrödinger equation in the presence of a monochromatic drive takes the form $|\psi_\alpha\rangle = e^{-i\epsilon_\alpha t}|u_\alpha(t)\rangle$ where $|u_\alpha(t)\rangle$ is periodic with $E^{(FER)} = \epsilon_\alpha - V_{bias} \pm \hbar\omega_L$.

Expanding these states in the unperturbed quantum-well basis yields $|u_\alpha(t)\rangle = \sum_n c_n^\alpha(t)|n\rangle$. Expressing the coefficients in a Fourier series $c_n^\alpha(t) = \sum_{m\in Z} a_{n,m}^\alpha e^{-i\omega_L t}$ and introducing the Sambe basis $|n\rangle\otimes|m\rangle$, we obtain the Floquet Hamiltonian in the extended Hilbert Space:

$$H_F = \sum_{n,m}(E_n - m\hbar\omega_L)|n,m\rangle\langle n,m| + \sum_{n,n',m} V_{n,n'}\,(|n,m\rangle\langle n',m+1| + |n,m\rangle\langle n',m-1|)$$

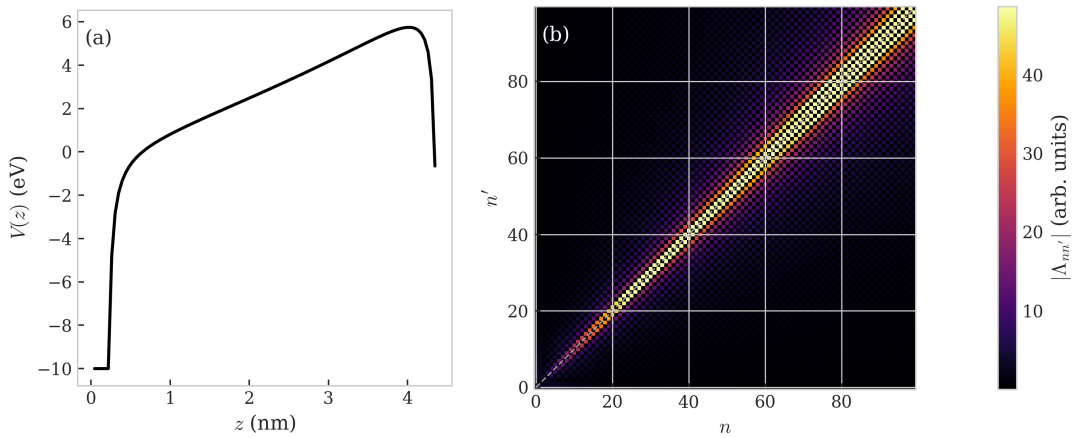

Figure S1. Modeling of FER states. a, *Effective one-dimensional potential profile of the tip–sample junction for a representative bias voltage.* ***b,*** *Magnitude of the overlap matrix elements between quantum well states, used to define the truncation criterion of the Hilbert space. The dominant contributions are concentrated near the diagonal, justifying the restriction to a finite number of states.*

The coupling matrix elements are defined as $V_{n,n'} = A_{cav}\Lambda_{n,n'}/2$, with $\Lambda_{n,n'} = \int \psi_n(z)\frac{d}{dz}\psi_{n'}(z)dz$. The resulting Hamiltonian is infinite-dimensional and therefore requires truncation. In practice the number of states is limited to $n \le n_{max}$, where we choose $n_{max} = 50$, which is justified by the fact that the coupling matrix decays rapidly with the difference $n - n'$, as shown in Fig. S1b. The number of sidebands is truncated to $|m| \le m_{max}$, where m_{max}=20 is set by the effective coupling strength relative to the driving energy scale, i.e. $\gamma A_0 \Lambda/(\hbar\omega_L)$ in the weak-to-intermediate regime.

The coupling matrix elements $\Lambda_{n,n'}$ are larger for states closer in energy, reflecting the fact that the momentum operator primarily couples neighboring levels. This formulation enables the numerical diagonalization of the Floquet Hamiltonian and the computation of laser-induced modifications of the tunneling spectrum.

To select the bright states in the illuminated case, we use the resonance condition where the energy of the system is replaced by the eigenvalues of the H_F. The number of eigenvalues equals that of the dark system times the number of replicas for each state. Unlike in the dark case, in the illuminated case the resonance condition can be met by

several eigenvalues of H_F precisely due to the replicas. To solve this redundancy problem, we choose to fold the eigenvalues in the interval $\left[\epsilon_1 - \frac{\hbar\omega_d}{2}, \epsilon_1 + \frac{\hbar\omega_d}{2}\right]$, where ϵ_1 is the first cavity state. We then restrict our analysis to the Floquet states whose quasienergies lie within this energy window. Therefore, we get a modified resonance condition with respect to the folded energies ϵ_α for the resonances in the presence of light $E^{(bright)} = \epsilon_\alpha - V_{bias} \pm m\hbar\omega_L$,

Each bright state is the result of one or more Floquet-Sambe states which satisfy this resonance condition. By projecting the resonant Floquet states onto the dark cavity state basis, it is possible to get a picture of which and how many states contribute, and whether there is hybridization between the dark cavity states. This can be quantified by the probabilities $P_n = \frac{1}{T}\int_0^T |c_n(t)|^2\, dt = \sum_m |a_{n,m}|^2$ of finding the electron in the dark cavity state n. In Fig. S2, we show these probabilities for the resonant Floquet states of Fig. 3 in the main text. This shows that whereas the peaks at $V_{bias} = 3.10\ V$ and at $V_{bias} = 4.40\ V$ are due to uncorrelated dark states coupled to the electromagnetic field, the measured bright resonance at $V_{bias} = 3.90\ V$ corresponds to a mixture of Floquet states, each of which is a superposition of Floquet-Sambe states.

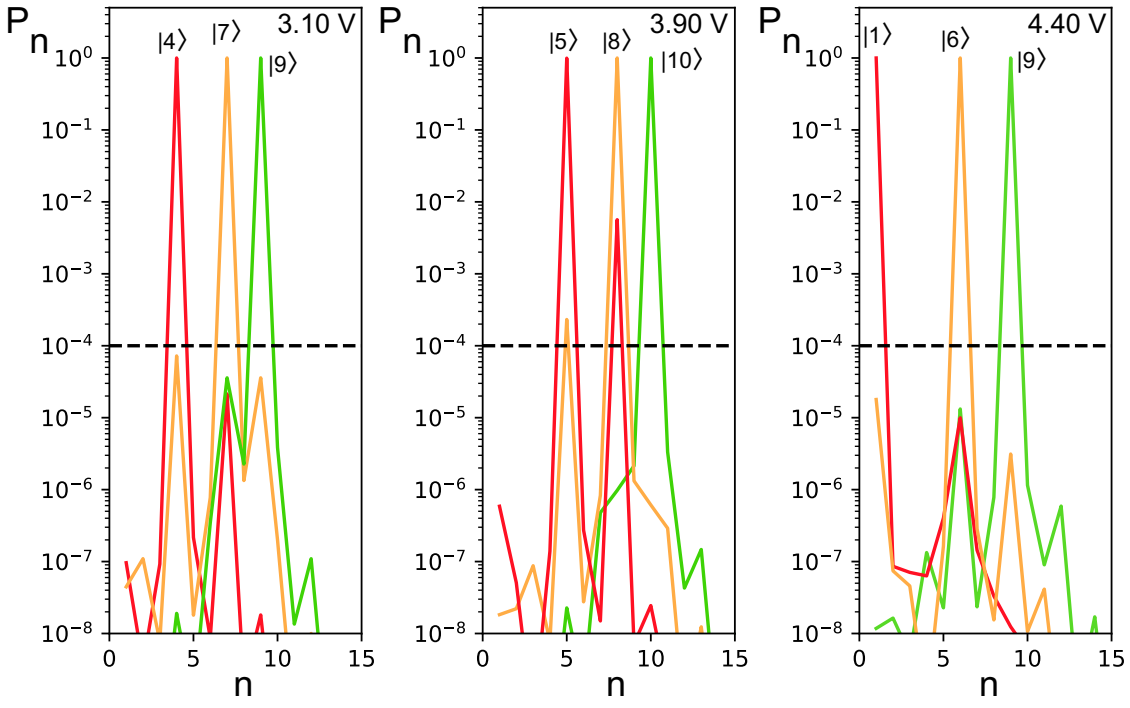

Figure S2. Probability of finding an electron in a dark cavity state*. Projection of Floquet states into the dark cavity basis for three representative energies. 3.10 V and 3.90 V correspond to the measured first and second bright states. 4.40 V corresponds to the measured first dark state. The red, orange, and green curves represent the probabilities for being in resonance with a Floquet state $\alpha = 1,2,3$ at the indicated voltages. The horizontal dashed line marks the probability threshold of 10^{-4} used for assigning which dark resonance contributes to each Floquet state.*

II. Tip-sample distance variation

Measuring tunneling spectra in constant-current mode inevitably induces changes in the tip-sample distance as a function of the applied bias voltage. The larger the bias, the wider

the cavity size. This translates into a different energy spacing between FERs due to the tilt of the confining potential, whose slope is controlled by the applied bias. This fact must be carefully considered when comparing the energies of different peaks in tunneling spectra, as different peaks (for either the dark or the illuminated cavity) are probed at different cavity sizes and, consequently, their energies may not be directly comparable. Notice how the energy-level spacing of the dark FERs changes notably across the three voltages shown in Fig. 3c of the main text. We have accounted for the tip-sample distance variation effect by incorporating the experimentally measured tip retraction in our Floquet model to calculate the peak positions for all the presented spectra.

III. Polarization dependence of the tunneling spectra

Fig. S3 shows in steps how the polarization dependence of the tunneling spectra for green excitation in Fig. 2a of the main text is obtained. First, the variation in relative tip-sample distance as a function of polarization is recorded, as shown in the graphs of Fig. S3a and the color plot in Fig. S3b. Then, the tunneling spectra are obtained by numerically deriving the Z(V) curves, as shown in the graphs in Fig. S3c and the color plot in Fig. S3d. The scattered points in Fig. S3d mark the positions of the bright and dark peaks obtained with our Floquet model. Fig. S4 shows the same protocol as detailed above for red excitation.

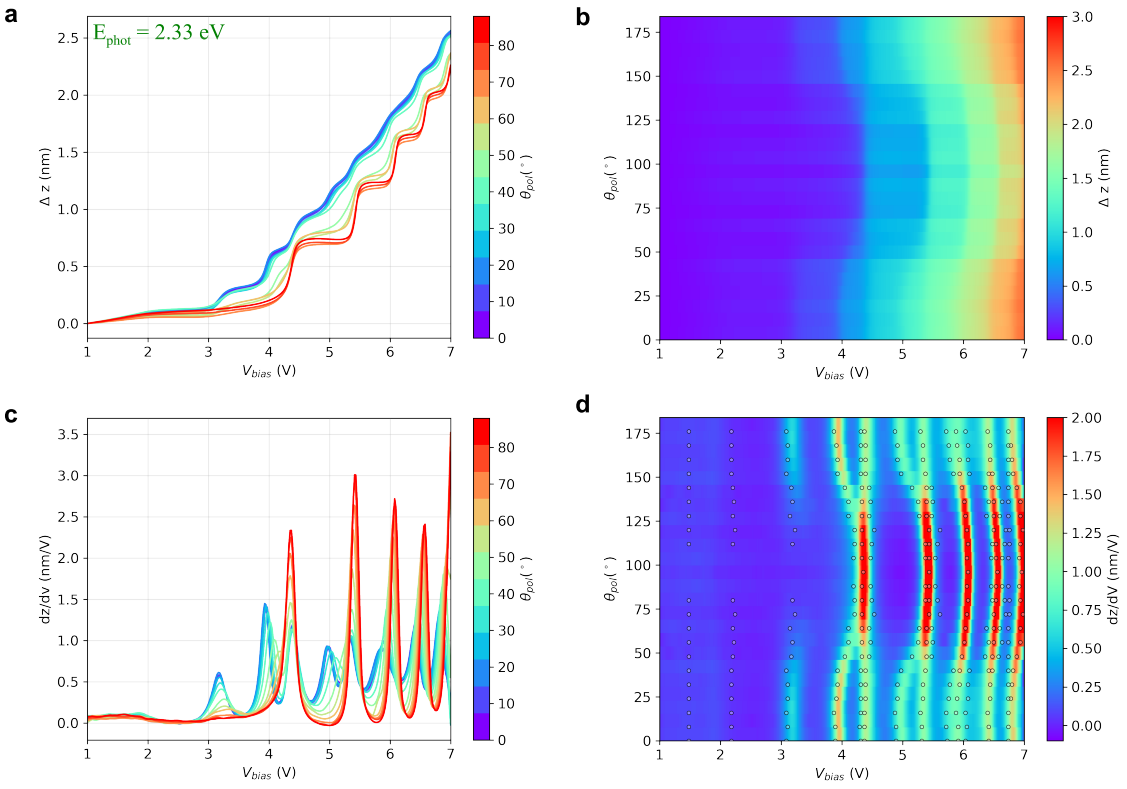

Figure S3. Polarization dependence of the tunneling spectra for green excitation. a, *Experimentally measured z(V) curves as a function of the angle of the laser linear polarization.* ***b,*** *Colormap representation of z(V) as a function of the linear polarization angle of the excitation laser.* ***c,*** *Tunneling spectroscopy dz/dV curves obtained by taking the numerical derivative of z(V) curves.* ***d,*** *Colormap representation of dz/dV as a function of the linear polarization angle of the excitation laser. The superimposed white circles mark the positions of the bright and dark peaks obtained with our Floquet model.*

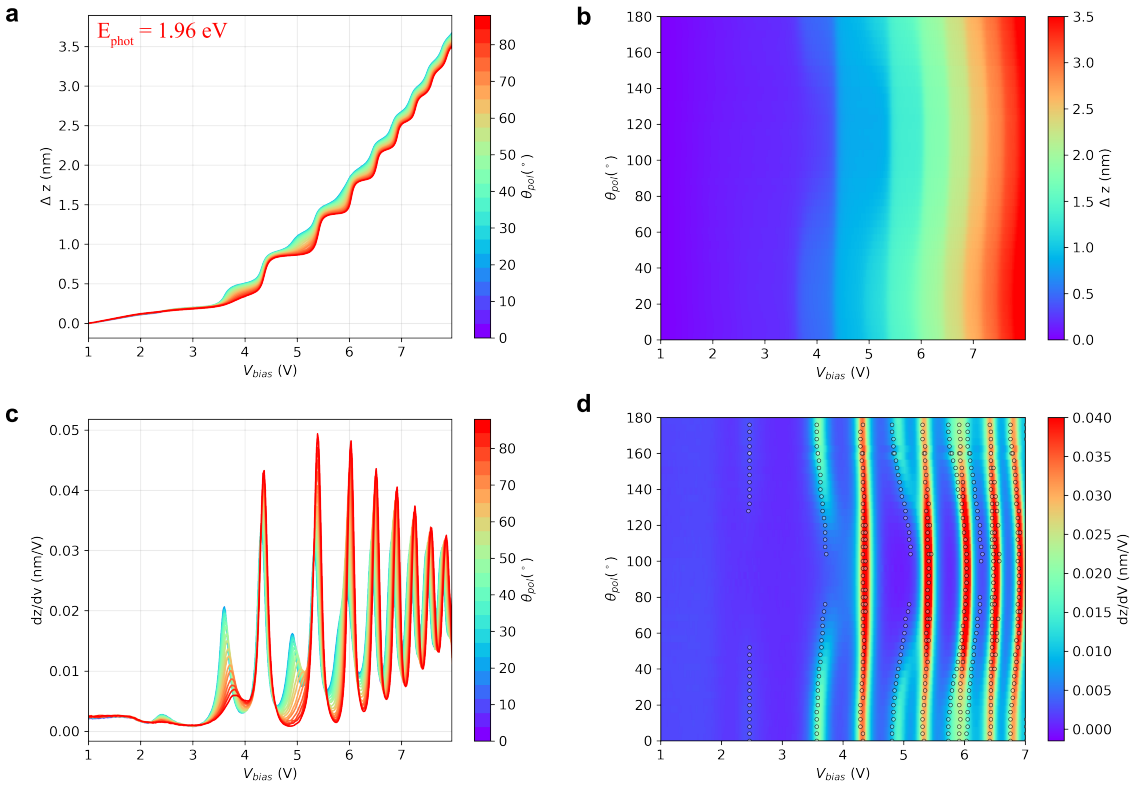

Figure S4. Polarization dependence of the tunneling spectra for red excitation. ***a,*** *Experimentally measured z(V) curves as a function of the angle of the laser linear polarization.* ***b,*** *Colormap representation of z(V) as a function of the linear polarization angle of the excitation laser.* ***c,*** *Tunneling spectroscopy dz/dV curves obtained by taking the numerical derivative of z(V) curves.* ***d,*** *Colormap representation of dz/dV as a function of the linear polarization angle of the excitation laser. The superimposed white circles mark the positions of the bright and dark peaks obtained with our Floquet model.*

Fig. S5 shows the intensity modulation of bright and dark states as a function of the laser polarization, in which the dark states peak when the bright ones vanish and vice versa.

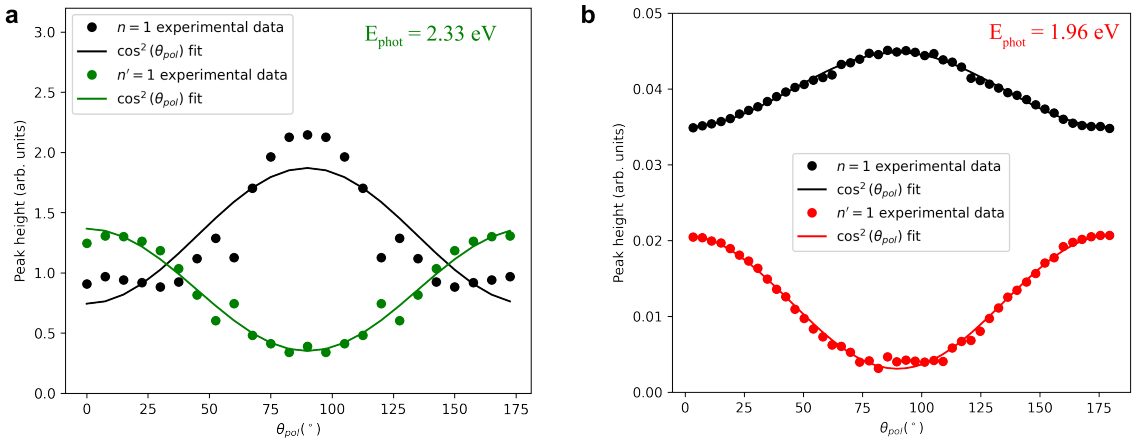

Figure S5. Polarization-selective intensity modulation. ***a,*** *Intensity modulation of the first bright state n'_1 and the first dark state n_1 as a function of the angle of the incident field for green driving. The dots correspond to experimental data, and the solid lines to the best possible fit to a $\cos^2(\theta_{pol})$ function.* ***b,*** *Intensity modulation for red driving.*

IV. Laser power dependence of the tunneling spectra

Fig. S5 shows in steps how the laser power dependence of the tunneling spectra for green excitation in Fig. 4c of the main text is obtained. First, the variation in relative tip-sample distance as a function of laser power is recorded, as shown in the graphs of Fig. S5a and the color plot in Fig. S5b. Then, the tunneling spectra are obtained by numerically deriving the Z(V) curves, as shown in the graphs in Fig. S5c and the color plot in Fig. S5d. The scattered points in Fig. S5d mark the positions of the bright and dark peaks obtained with our Floquet model. Fig. S6 shows the same protocol as detailed above for red excitation.

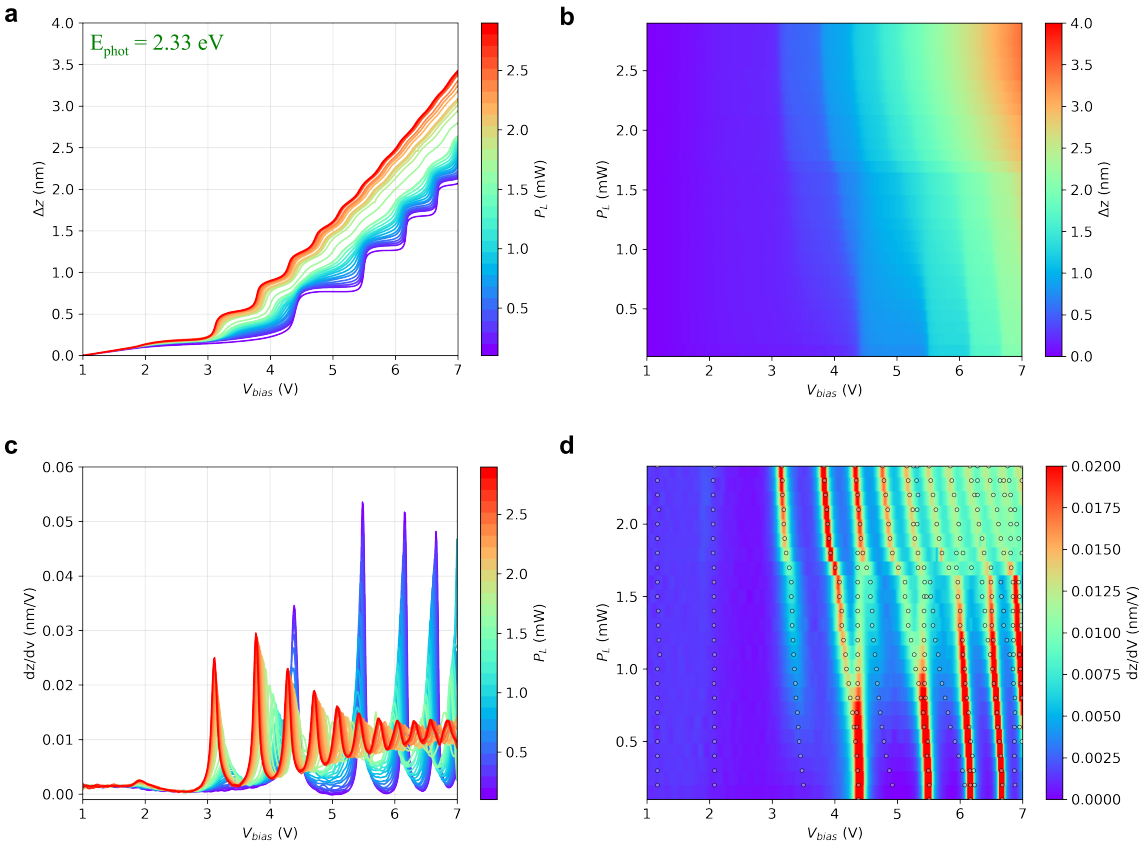

Figure S6. Laser power dependence of the tunneling spectra for green excitation. ***a,*** *Experimentally measured z(V) curves as a function of the laser power.* ***b,*** *Colormap representation of z(V) as a function of the laser power.* ***c,*** *Tunneling spectroscopy dz/dV curves obtained by taking the numerical derivative of z(V) curves.* ***d,*** *Colormap representation of dz/dV as a function of the laser power. The superimposed white circles mark the positions of the bright and dark peaks obtained with our Floquet model.*

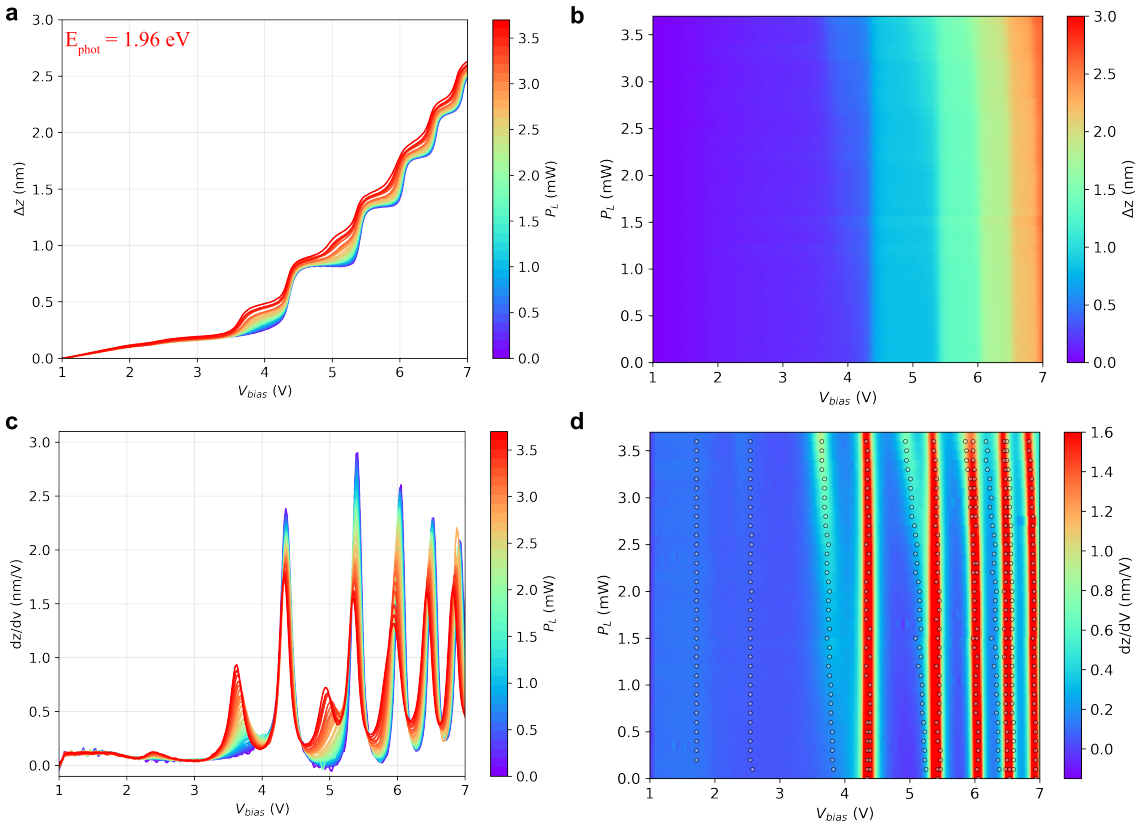

Figure S7. Laser power dependence of the tunneling spectra for red excitation. a, *Experimentally measured z(V) curves as a function of the laser power.* ***b,*** *Colormap representation of z(V) as a function of the laser power.* ***c,*** *Tunneling spectroscopy dz/dV curves obtained by taking the numerical derivative of z(V) curves.* ***d,*** *Colormap representation of dz/dV as a function of the laser power. The superimposed white circles mark the positions of the bright and dark peaks obtained with our Floquet model.*

V. Current dependence of the tunneling spectra

Fig. S7 shows in steps how the current dependence of the tunneling spectra for green excitation in Fig. 4a of the main text is obtained. First, the variation in relative tip-sample distance as a function of tunneling current is recorded, as shown in the graphs of Fig. S7a and the color plot in Fig. S7b. Then, the tunneling spectra are obtained by numerically deriving the Z(V) curves, as shown in the graphs in Fig. S7c and the color plot in Fig. S7d. The scattered points in Fig. S7d mark the positions of the bright and dark peaks obtained with our Floquet model. Fig. S8 shows the same protocol as detailed above for red excitation.

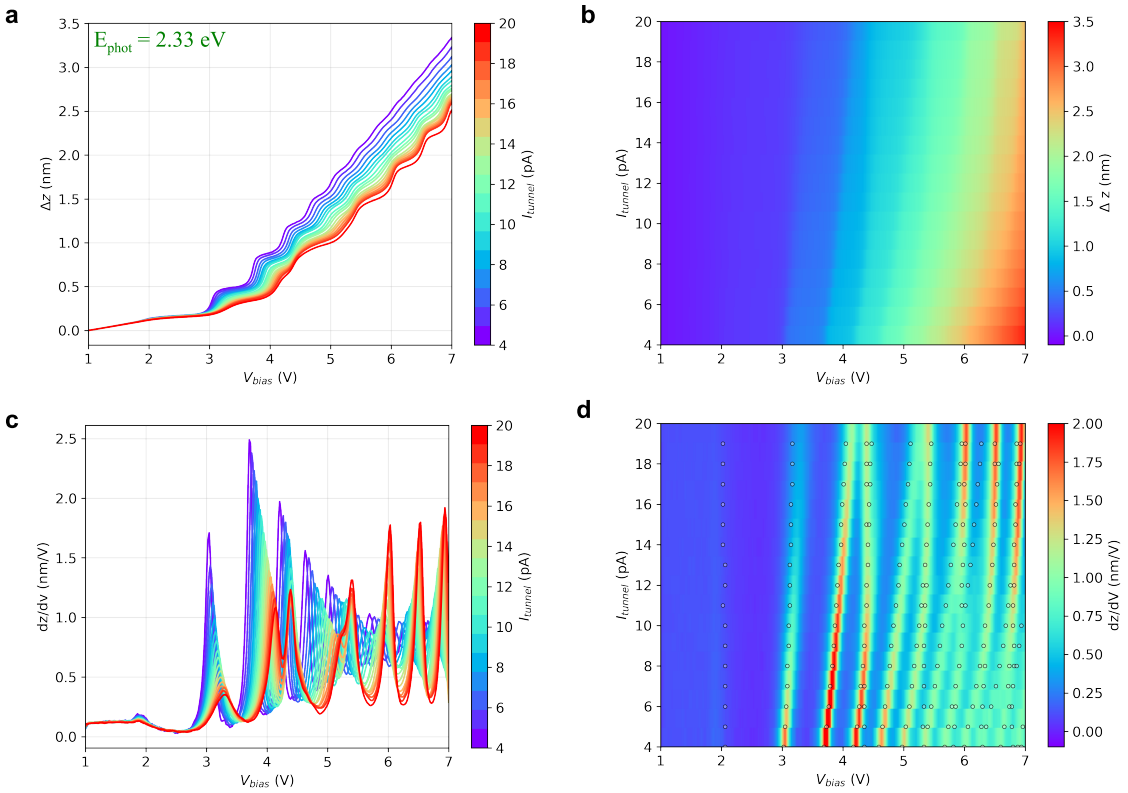

Figure S8. Current dependence of the tunneling spectra for green excitation. a, *Experimentally measured z(V) curves as a function of the tunneling current setpoint.* ***b,*** *Colormap representation of z(V) as a function of the tunneling current.* ***c,*** *Tunneling spectroscopy dz/dV curves obtained by taking the numerical derivative of z(V) curves.* ***d,*** *Colormap representation of dz/dV as a function of the tunneling setpoint. The superimposed white circles mark the positions of the bright and dark peaks obtained with our Floquet model.*

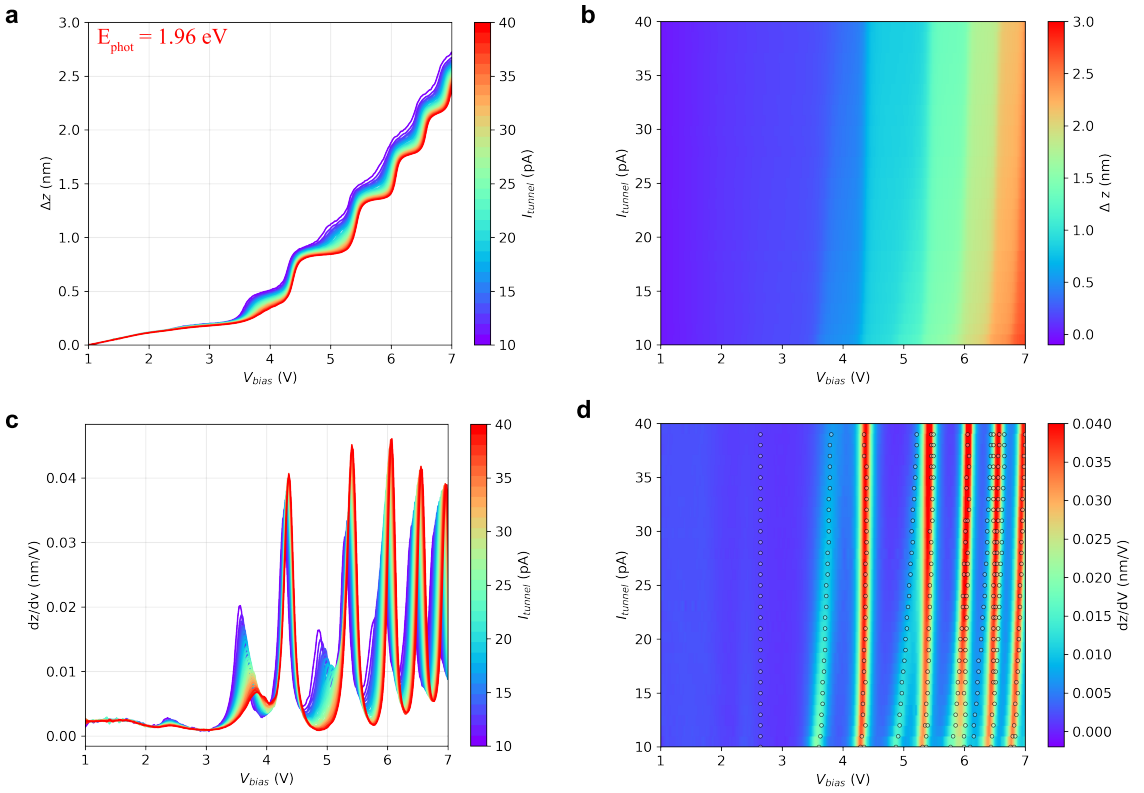

Figure S9. Current dependence of the tunneling spectra for red excitation. a, *Experimentally measured z(V) curves as a function of the tunneling current setpoint.* ***b,*** *Colormap representation of z(V) as a function of the tunneling current.* ***c,*** *Tunneling spectroscopy dz/dV curves obtained by taking the numerical derivative of z(V) curves.* ***d,*** *Colormap representation of dz/dV as a function of the tunneling setpoint. The superimposed white circles mark the positions of the bright and dark peaks obtained with our Floquet model.*

VI. Tunneling spectra with different tips

To rule out the possibility that the emergence of Floquet states is dictated by the precise tip shape or material, we have measured bright and dark spectra using six different tips: three Au and three Ag. The results are summarized in Fig. S10. Three spectra were measured with red excitation (Figs. S10 a-c) and three with green excitation (Figs. S10 d-f). While the exact number and positions of peaks in the dark tunneling spectra depend on the tip-sample confining potential, which is determined by the tip shape, the emergence of bright states is independent of the tip shape or material. The photon energy selects which dark states hybridize with the laser field, thereby determining the appearance and separation between bright states. We hypothesize that the plasmonic response of the cavity, shown as an inset in each graph, along with a dashed vertical line at the driving laser energy, may account for the differences in the relative heights of the bright peaks.

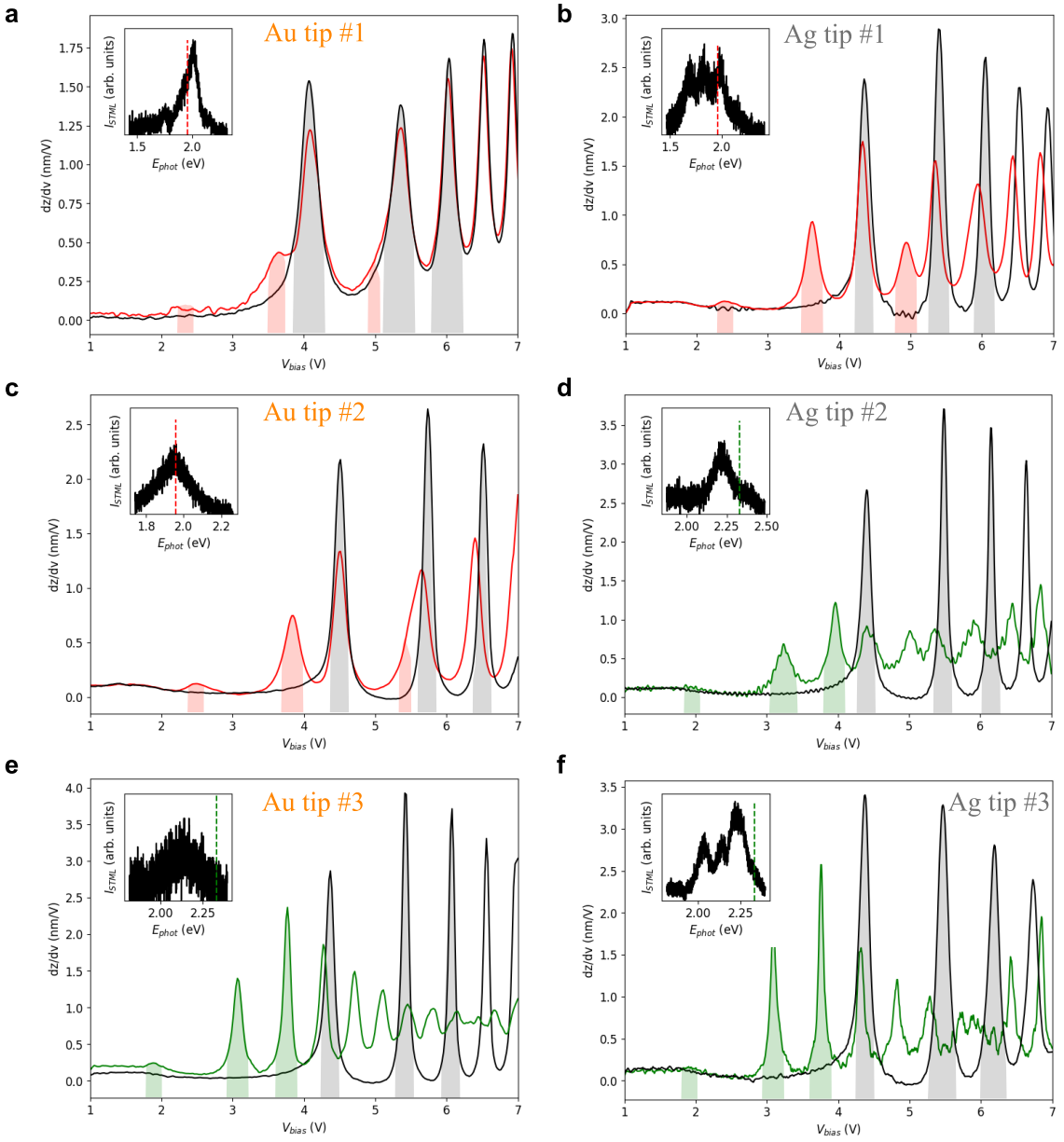

Figure S10. Tunneling spectroscopy with different STM tips and excitation lasers. a-c, *Bright and dark tunneling spectra for the red excitation laser for three different tips.* ***d-f,*** *Bright and dark tunneling spectra for the green excitation laser for three different tips. The inset of each graph corresponds to the plasmonic response of the cavity measured by electroluminescence.*

References

1. F. Dall'Agnol, F. & P. Mammana, V. Solution for the electric potential distribution produced by sphere-plane electrodes using the method of images. *Revista Brasileira de Ensino de Física* **31**, (2009).

2. Martinez-Blanco, J. & Fölsch, S. Light emission from Ag(111) driven by inelastic tunneling in the field emission regime. *Journal of Physics Condensed Matter* **27**, (2015).